Multiphoton ionization and high-order harmonic generation of He, Ne, and Ar atoms in intense pulsed laser fields: Self-interaction-free time-dependent density-functional theoretical approach

Xiao-Min Tong* and Shih-I Chu

Department of Chemistry, University of Kansas, and Kansas Center for Advanced Scientific Computing, Lawrence, Kansas 66045
(Received 22 December 2000; published 12 June 2001)

We present a detailed study of the multiphoton ionization and high-order harmonic generation (HHG) processes of rare-gas atoms (He, Ne, and Ar) in intense pulsed laser fields by means of a *self-interaction-free* time-dependent density-functional theory (TDDFT) recently developed. The time-dependent exchange-correlation potential with proper short- and long- range potential is constructed by means of the *time-dependent optimized effective potential* (TDOEP) method and the incorporation of an explicit *self-interaction-correction* (SIC) term. The TDOEP-SIC equations are solved accurately and efficiently by the *time-dependent generalized pseudospectral* technique. In this study, all the valence electrons are treated explicitly and nonperturbatively and their partial contributions to the ionization and HHG are analyzed. The results reveal instructive and qualitatively different behavior from each subshell orbital. Moreover, we found that the HHG yields from Ne and Ar atoms are considerably larger than that of the He atom in strong fields. Three main factors are identified for accounting the observed phenomena: (a) the binding energy of the subshell valence electron, (b) the orientation of the valence electron orbital (with respect to the electric-field polarization), and (c) the effect of multiphoton resonant excitation. In particular, we found that the np_0 valence electrons (in Ne and Ar) with lowest binding energies and electron orbital orientation parallel to the electric-field direction, make the dominant contributions to both ionization and HHG processes in sufficiently strong fields.

I. INTRODUCTION

The study of atomic and molecular multiphoton and high-order nonlinear optical processes is a subject of much current interest and significance in science and technology [1]. In particular, multiple high-order harmonic generation (HHG) is one of the most rapidly developing topics in strong-field atomic and molecular physics. The generation of harmonics of orders in excess of 300 from rare-gas atoms has been recently demonstrated by experiments [2–4] using laser pulses shorter than 20 fs and peak intensity more than 10^{14} W/cm^2. The shortest wavelength generated by the HHG mechanism to date is about 2.7 nm [2–4], well into the water window regime. To describe such intense-field processes using an *ab initio* wave-function approach, it is necessary to solve the time-dependent Schrödinger equations of many-electron systems, which is well beyond the capability of current supercomputer technology. One of the successful approximations being used is the *single-active-electron* (SAE) model with frozen core [5,6]. The SAE model has been applied to the study of HHG of rare-gas atoms in linearly polarized (LP) laser fields (involving *two* spatial dimensions), providing useful insights regarding atomic multiphoton dynamics. However, within the SAE approach, the electron correlation and the contribution and the role of the individual spin orbital, particularly those in the valence shell, cannot be explicitly treated. Indeed the dynamical role of the individual valence electron to the HHG and multiphoton ion-

ization processes in strong fields has not been thoroughly studied before. Such a study can provide insights regarding the detailed quantum dynamics and HHG mechanisms, as well as the optimal control of strong-field processes. In this paper we present a quantum study of multiphoton ionization and HHG processes of rare-gas atoms (He, Ne, and Ar) by means of the *self-interaction-free* time-dependent density-functional theory (TDDFT) recently developed [7,8].

It is known that the conventional steady-state DFT and TDDFT using explicit exchange-correlation (xc) energy functionals, such as those from the local spin-density approximation (LSDA) [9] and generalized gradient approximation (GGA) [10–12], contain spurious self-interaction energy and the xc potentials do not have the proper long-range Coulombic tail $-1/r$. As a result, while the total electron energies of the ground states of atoms and molecules are rather accurate, the excited and resonance states, as well as the ionization potentials (from the highest-occupied orbital energies) are less satisfactory. For example, the atomic ionization potentials calculated from the conventional DFT approach using the LSDA or GGA energy functionals are typically 30 to 50 % too low. Recently, we have presented a self-interaction-free DFT [13] based on the extension of the KLI's (Krieger-Li-Iafrate) original treatment [14] of the optimized effective potential (OEP) formalism [15,16] along with the implementation of an explicit self-interaction-correction (SIC) term [13,17]. Such an OEP/KLI-SIC method uses only *orbital-independent* single-particle *local* potentials that are self-interaction free and have the proper short- and long-range ($-1/r$) behavior and is capable of providing reasonably high accuracy for the excited states and ionization potentials (well within a few percent of the experimental values) across the periodic table [18]. Further it is

---

*Present address: ''Cold Trapped Ions'' Project, ICORP, JST, Axis Chofu Bdg 3F, 1-40-2 Fuda, Chofu, Tokyo 182-0024 Japan. Email address: tong@hci.jst.go.jp

shown that the autoionizing resonances can be adequately described by the OEP/KLI-SIC procedure within the experimental error [13]. A similar procedure has been used recently for the study of static and dynamical properties of metal clusters [19]. In the present dynamical study, we shall use the TDDFT with OEP/SIC, which is the extension of the steady-state OEP/KLI-SIC method to the time domain [7,8]. We note that a related time-dependent KLI theory has been proposed by Ullrich *et al.* [20] without using the explicit SIC form. In this latter work [20], the Hartree-Fock (*nonlocal*) exchange energy functional is used in the construction of the time-dependent optimized effective potential. In the present paper, only orbital-independent single-particle *local* potential is involved for each time step and is thus computationally more efficient, and yet similar high accuracy is maintained. The time-dependent OEP/KLI-SIC equations in the present approach can be solved accurately and efficiently by means of the *time-dependent generalized pseudospectral* (TDGPS) method [21] recently developed for precision calculations of HHG [21–24] and Rydberg-atom high-resolution spectroscopy in external fields [25,26].

This paper is organized as follows. In Sec. II, we briefly outline the TDDFT/OEP-SIC equations and TDGPS method. In Sec. III, we present the calculated results of multiphoton ionization of rare-gas atoms from individual valence electrons and discuss the possible mechanisms responsible for the observed phenomena. In Sec. IV, we present the corresponding results and analysis for the HHG processes. This is followed by a conclusion in Sec. V.

II. SELF-INTERACTION-FREE TIME-DEPENDENT DENSITY-FUNCTIONAL THEORY

In this section, we briefly outline the main working equations of the time-dependent density-functional theory (TD-DFT) with optimized effective potential (OEP) and self-interaction correction (SIC) recently developed for nonperturbative treatment of multiphoton processes of atoms in intense laser fields [7,8]. The main time-dependent OEP/KLI-SIC equation [7,8] can be expressed as (in atomic units):

$$i \frac{\partial}{\partial t} \psi_{i\sigma}(\mathbf{r},t) = \hat{H}(\mathbf{r},t) \psi_{i\sigma}(\mathbf{r},t)$$

$$= \left[-\frac{1}{2} \nabla^2 + V_{SIC,\sigma}^{OEP}(\mathbf{r},t) \right] \psi_{i\sigma}(\mathbf{r},t)$$

$$i = 1,2,\ldots,N_\sigma. \quad (1)$$

Here, $V_{SIC,\sigma}^{OEP}(r,t)$ is the time-dependent OEP with SIC determined in such a way that the time-dependent spin-orbital wave functions $\{\psi_{i\sigma}(\mathbf{r},t)\}$ render the total action functional $A[\{\psi_{i\sigma}(\mathbf{r},t)\}]$ stationary [7,8,20], i.e.,

$$\frac{\delta A[\{\psi_{i\sigma}(\mathbf{r},t)\}]}{\delta V_{SIC,\sigma}^{OEP}(\mathbf{r},t)} = 0. \quad (2)$$

This gives rise to the following expression for $V_{SIC,\sigma}^{OEP}(\mathbf{r},t)$ [7],

$$V_{SIC,\sigma}^{OEP}(\mathbf{r},t) = v_{ext}(\mathbf{r},t) + \int \frac{\rho(\mathbf{r}',t)}{|\mathbf{r}-\mathbf{r}'|} d^3\mathbf{r}' + V_{xc,\sigma}^{SIC}(\mathbf{r},t). \quad (3)$$

Here, $V_{xc,\sigma}^{SIC}(\mathbf{r},t)$ has the following form [7]:

$$V_{xc,\sigma}^{SIC}(\mathbf{r},t) = \sum_i \frac{\rho_{i\sigma}(\mathbf{r},t)}{\rho_\sigma(\mathbf{r},t)} \{v_{i\sigma}(\mathbf{r},t) + [\bar{V}_{xc,i\sigma}^{SIC}(t) - \bar{v}_{i\sigma}(t)]\}, \quad (4)$$

$$v_{i\sigma}(\mathbf{r},t) = \frac{\delta E_{xc}^{SIC}[\rho_\uparrow,\rho_\downarrow]}{\delta \rho_{i\sigma}(\mathbf{r},t)}$$

$$= \frac{\delta E_{xc}[\rho_\uparrow,\rho_\downarrow]}{\delta \rho_\sigma(\mathbf{r},t)} - \int \frac{\rho_{i\sigma}(\mathbf{r}',t)}{|\mathbf{r}-\mathbf{r}'|} d^3\mathbf{r}' - \frac{\delta E_{xc}[\rho_{i\sigma},0]}{\delta \rho_{i\sigma}(\mathbf{r},t)}, \quad (5)$$

and

$$\bar{V}_{xc,i\sigma}^{SIC}(t) = \langle \psi_{i\sigma} | V_{xc\sigma}^{SIC}(\mathbf{r},t) | \psi_{i\sigma} \rangle, \quad (6)$$

$$\bar{v}_{i\sigma}(t) = \langle \psi_{i\sigma} | v_{i\sigma}(\mathbf{r},t) | \psi_{i\sigma} \rangle. \quad (7)$$

In deriving the above equations, use has been made of the following SIC expression for the exchange-correlational action functional A_{xc}^{SIC}

$$A_{xc}^{SIC} = \int_{-\infty}^{t'} dt\, E_{xc}^{SIC}[\{\rho_{i\sigma}(\mathbf{r},t)\}], \quad (8)$$

where $E_{xc}^{SIC}[\{\rho_{i\sigma}(\mathbf{r},t)\}]$ is the SIC version of any given explicit xc energy functional E_{xc}, such as LSDA, Becke-Lee-Yang-Parr (BLYP) [10,11], etc.,

$$E_{xc}^{SIC}[\{\rho_{i\sigma}\}] = E_{xc}[\rho_\uparrow,\rho_\downarrow] - \sum_\sigma \sum_{i=1}^{N_\sigma} \{J[\rho_{i\sigma}] + E_{xc}[\rho_{i\sigma},0]\}. \quad (9)$$

We can now construct the TD-OEP/SIC through Eqs. (2)–(9) and solve Eq. (1) for the individual time-dependent spin-orbital wave function in a self-consistent manner. The single-particle time-dependent OEP/SIC so constructed is a local potential (for every time step) and has the correct long-range potential behavior.

To solve Eq. (1), we use the time-dependent generalized pseudospectral (TDGPS) method [21] that consists of the following two essential steps: (a) The generalized pseudospectral technique [27,28] is used for *nonuniform* and optimal spatial grid discretization of the spatial coordinates. (b) A second-order split-operator technique in the *energy representation* [21] is used for the efficient and accurate time propagation of the wave function. The method has been shown to be capable of providing a highly accurate time-dependent wave function for both HHG calculations [21] and high-resolution spectroscopy of field-induced Rydberg atoms [25,26] with the use of only a modest number of spatial grid

points. Moreover, the use of the energy representation facilitates the elimination of undesirable high-energy (fast oscillating) components, allowing the use of considerably larger time step in time propagation and the independent time propagation of each individual partial-wave wave function. Detailed numerical procedure is given elsewhere [7,8,21].

Once the individual time-dependent spin-orbital wave functions $\{\psi_{i\sigma}(t)\}$ are obtained, we can calculate the time-dependent induced dipole moment as follows:

$$d(t) = \int z\rho(\mathbf{r},t)d\mathbf{r} = \sum_{i\sigma} d_{i\sigma}(t), \qquad (10)$$

where

$$d_{i\sigma}(t) = n_{i\sigma}\langle\psi_{i\sigma}(t)|z|\psi_{i\sigma}(t)\rangle, \qquad (11)$$

is the induced dipole of ith spin orbital, and $n_{i\sigma}$ is its electron occupation number. The high-harmonic generation (HHG) power spectrum can now be obtained by means of the Fourier transform of the time-dependent induced dipole moment:

$$P(\omega) = \left|\frac{1}{t_f - t_i}\int_{t_i}^{t_f} d(t)e^{-i\omega t}\right|^2 = |d(\omega)|^2. \qquad (12)$$

Finally, the time-dependent (muitiphoton) ionization probability of the ith spin orbital can be calculated according to

$$P_{i\sigma}(t) = 1 - N_{i\sigma}(t), \qquad (13)$$

where

$$N_{i\sigma}(t) = \langle\psi_{i\sigma}(t)|\psi_{i\sigma}(t)\rangle \qquad (14)$$

is the time-dependent population (survival probability) of the ith spin-orbital.

III. MULTIPHOTON IONIZATION OF RARE-GAS ATOMS

We first consider the ionization processes of rare-gas atoms (He, Ne, and Ar) with intense linearly polarized (LP) short pulsed laser fields. In the electric-dipole approximation, the atom-field interaction has the following form:

$$V(t) = -\mathbf{r}\cdot\mathbf{E}_0 f(t)\sin(\omega t), \qquad (15)$$

where E_0 is the electric-field amplitude, $f(t)$ is the laser pulse shape, and ω is the laser frequency. For all the calculations reported below, the laser wavelength used is 1064 nm, and the pulse length used is 60 optical cycles with $\sin^2$ pulse shape.

In the present paper, our main focus is on the response of the individual valence electron to the intense laser fields. The LSDA exchange-correlation energy functional [9] is used in Eqs. (5), (8), and (9) for the construction of time-dependent OEP. Under the laser intensity range $(5\times10^{13}$ to 4×10^{14} W/cm^2) considered in this paper, we found the inner-shell electrons do not participate appreciably in the multiphoton processes. Thus, to a good approximation, the inner-shell electrons can be frozen. Note that such a frozen-core
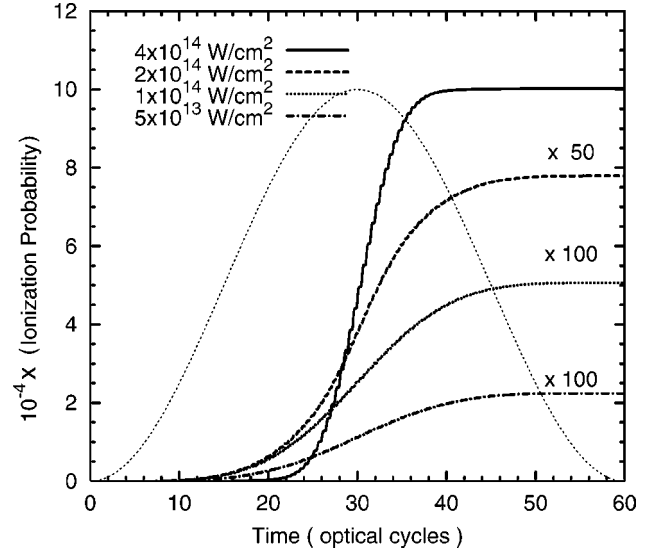

FIG. 1. The ionization probability of He atoms in pulsed laser fields with peak intensity: (a) 5×10^{13} W/cm^2, (b) 10^{14} W/cm^2, (c) 2×10^{14} W/cm^2, and (d) 4×10^{14} W/cm^2. The laser field has $\sin^2$ pulse shape with 60 optical cycles in pulse length and the wavelength used is 1064 nm.

approximation is different from that of SAE, since in the present case, all the valence electrons are treated explicitly and each contributes to the total effective potential and multiphoton processes in a qualitatively different way as to be explored below.

A. Multiphoton ionization of He, Ne, and Ar atoms

Figure 1 shows the time-dependent total ionization probabilities of He at four different laser peak intensities, indicating that the ionization probability increases rapidly as the peak intensity is increased. Also shown in Fig. 1 is the laser pulse shape (dotted line). For each case, as the laser field approaches its peak intensity, the ionization probability from the $1s$ orbital increases rapidly and reaches the maximum. Beyond the peak intensity, the ionization rate begins to slow down, partly due to the decrease of the laser intensity and partly due to the fact that a partially ionized atom will become more difficult (than the parent neutral atom) to detach the remaining electrons.

Figures 2(a)–2(d) show, respectively, the partial time-dependent ionization probabilities of the Ne atom from its individual valence electron orbital ($2s$, $2p_1$, and $2p_0$) at four different laser peak intensities. Note that due to the cylindrical symmetry, the response of $2p_1$ and $2p_{-1}$ orbitals to the LP laser fields is identical. Thus, in the following, all the $2p_1$ results refer to the total contributions due to both $2p_1$ and $2p_{-1}$ orbitals. [The $1s$ orbital is tightly bound by the nucleus and its contribution to the total ionization probability and HHG are negligible.] For field-free Ne atoms, the $2p_0$ and $2p_1$ electrons are less bound by the nucleus than the $2s$ orbital. As the laser field is polarized in the z direction, one expects that the $2p_0(=2p_z)$ electrons will be most easily ionized, followed by the $2p_1$ electrons and then the $2s$ electrons. Surprisingly, we found that the $2s$ level (whose bind-
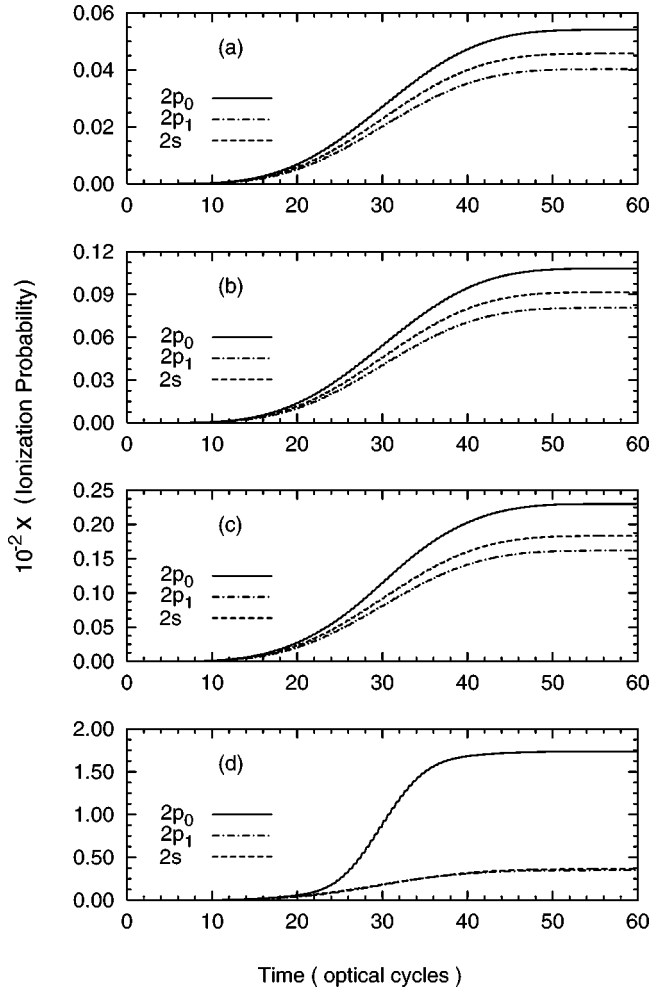
FIG. 2. The ionization probabilities of $2s$, $2p_0$, and $2p_1$ valence electrons of Ne atoms in pulsed laser fields. The laser intensities (a)–(d) and other laser parameters used are the same as those in Figs. 1(a)–1(d).
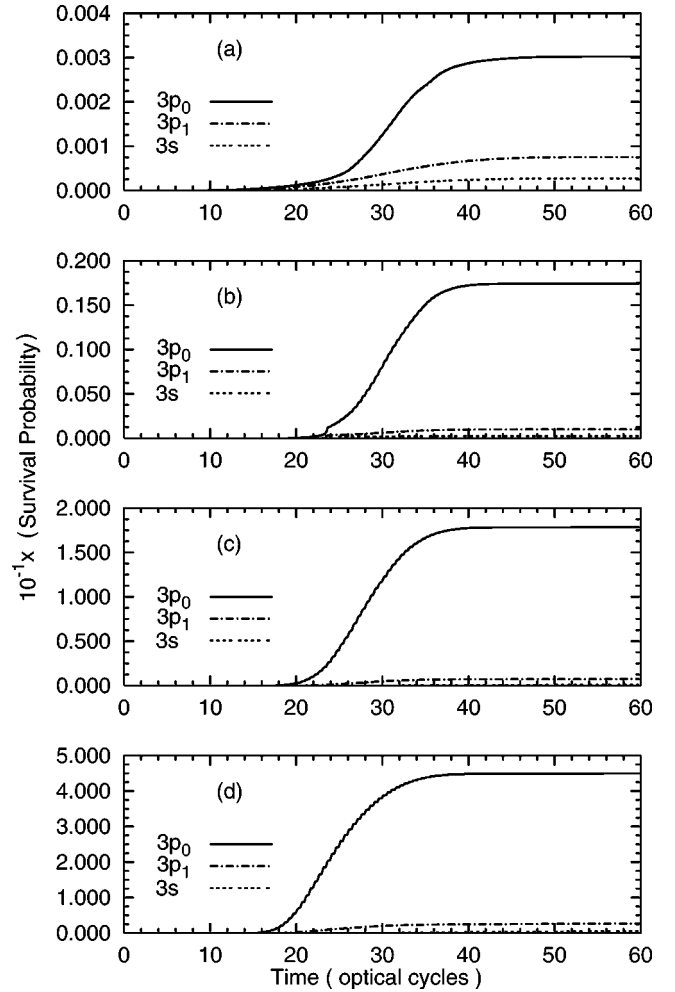

FIG. 3. The ionization probabilities of $3s$, $3p_0$, and $3p_1$ valence electrons of Ar atoms in pulsed laser fields. The laser intensities (a)–(d) and other laser parameters used are the same as those in Figs. 1(a)–1(d).

ing energy is about twice that of $2p$ levels) is the second easiest ionized orbital, particularly at lower intensities, (a)–(c). As the laser peak intensity further increases [Fig. 2(d)], the ionization probabilities of $2s$ and $2p_1$ merge to each other.

Figures 3(a)–3(d) show, respectively, the partial time-dependent ionization probabilities of the Ar atom from its individual valence electron orbital ($3s$, $3p_1$, and $3p_0$) at four different laser peak intensities. [The inner-shell electrons are frozen since they are tightly bound by the nucleus and do not make appreciable contributions to the ionization or HHG processes.] Different from the Ne atom case, here we found that the $3p_1$ electrons are easier to ionize than the $3s$ electrons, as expected from the consideration of the binding energy alone.

B. Ionization mechanisms of valence electrons in rare-gas atoms

Since the ionization behavior of the valence electrons in Ne and Ar atoms is somewhat different, we discuss below the physical mechanisms responsible for the ionization pro-

cesses. For the valence electrons, there are three main factors that can affect the ionization probability of individual sub-shell electron: (a) the binding energy or ionization potential of the orbital: the smaller the binding energy, the larger the ionization probability; (b) the orientation of the orbital. In general, the electron orbital with its electron density parallel to the laser- (electric-) field direction has a larger probability to be ionized. Similar effect has been observed in the microwave ionization of Rydberg atoms [29]; (c) the multiphoton resonant excitation effect that can lead to the enhancement of the ionization rate.

Now for the ns and np valence electrons of rare-gas atoms, the binding energies of ns electrons are larger than that of np_1 and np_0 electrons. [Note that the field-free binding energy of np_0 orbital is identical to that of np_1 orbital.] Thus, based on the binding energy consideration alone, one expects to see that np_0 and np_1 electrons are easier to ionize than the ns electrons. However, if the orbital orientation alone is taken into account, then one expects to see that np_0 orbital (with the electron density parallel to the electric field) is the one easiest to ionize, while the np_1 orbital (with the
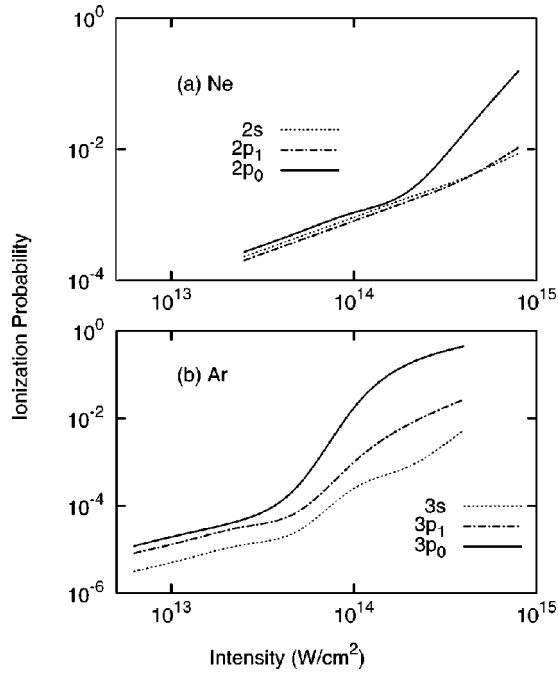
FIG. 4. The valence-electron subshell ionization probabilities at the end of the laser pulse as a function of laser peak intensity for (a) Ne, and (b) Ar. The laser wavelength used is 1064 nm and the pulse length is 60 optical cycles.

FIG. 5. The HHG power spectra of He, Ne, and Ar atoms in pulsed laser fields with peak intensities: (a) 5×10^{13} W/cm^2, and (b) 4×10^{14} W/cm^2. The laser parameters uses are 1064 nm, sin^2 pulse shape and 60 optical cycles in pulse length.

electron density perpendicular to the electric field) is the most difficult one to ionize. Thus, it is clear that the np_0 valence electron will always be the easiest one to detach, while the relative ionization probability of the np_1 and ns electrons will depend upon the relative importance of the binding energy and orientation factors, as well as the possible enhancement due to accidental multiphoton resonant excitation. In general, we found that in the absence of multiphoton resonant excitation, the np_1 orbital ionization rate is higher than that of the ns orbital. This is evident in Fig. 3 for Ar. Since there is a resonant excitation from $2s$ to $2p_0$ by 19 photons, the $2s$ ionization rate is larger than that of $2p_1$ for the case of Ne atoms. Such resonant structure is more clearly seen in the HHG contribution by the individual orbital, which will be discussed in the next section. Note also that the ionization probability of Ar atoms increases rather rapidly near the laser peak intensity as shown in Fig. 3. On the other hand, the ionization probability of Ne atoms increase less rapidly around the laser peak intensity as shown in Fig. 2.

The laser peak intensity can also play some role in the relative order of orbital ionization. In Figures 4(a)-4(b), we extend the calculations to higher laser peak intensities for Ne and Ar, respectively. Indeed we find that the $2p_1$ orbital in Ne is now easier to detach than the $2s$ orbital at the highest-intensity range considered. However, there is no change of order in Ar. This indicates that the binding energy factor prevails at the higher-intensity regime, although the orientation and resonant effects are still important to consider.
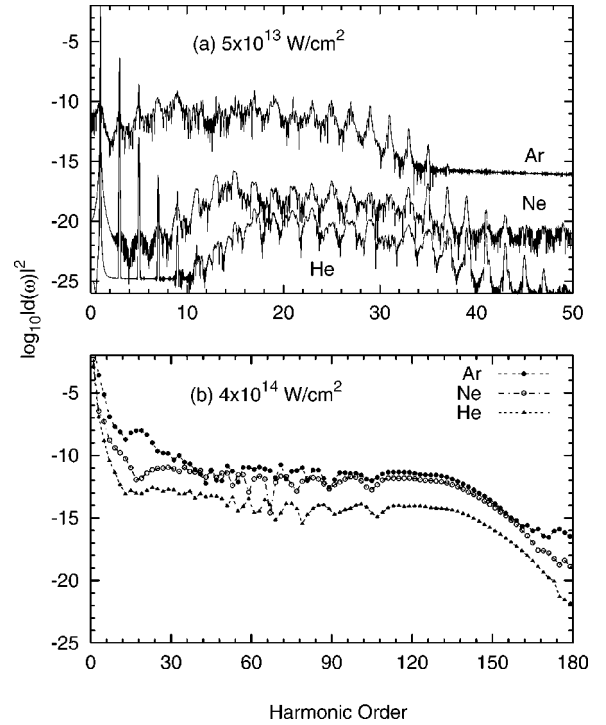
IV. MULTIPLE HIGH-ORDER HARMONIC GENERATION OF RARE-GAS ATOMS

We now consider the multiple high-order harmonic generation (HHG) processes of rare-gas atoms in intense pulsed laser fields. Figures 5(a) and 5(b) show the comparison of the HHG power spectrum of He, Ne, and Ar at a laser peak intensity equal to 5×10^{13} and 4×10^{14} W/cm^2, respectively. The ionization potentials, I_p, of He, Ne, and Ar are, respectively, 24.97, 21.97, and 14.94 eV. As shown in Fig. 5(a), the smaller the ionization potential of the atom, the larger the HHG yield, but the shorter the harmonic cutoff frequency. Thus, Ar has the largest HHG yield and the shortest cutoff frequency, while He has the smallest HHG yield but the longest HHG plateau and cutoff frequency. The cutoff harmonic position may be estimated by the two-step quasiclassical model [30,31] in the tunneling limit, and in not-so-strong laser fields: $n_{cutoff} = (I_p + 3.17 U_p)/\omega$, with I_p the ionization potential and U_p the ponderomotive energy. Figure 5(b) shows that as the laser field becomes sufficiently strong, the HHG yield and the cutoff position of rare-gas atoms will get closer to each other, indicating that the effect of the ionization potential is getting smaller. Another salient feature in Fig. 5(b) is that the power spectrum of Ar and Ne are considerably closer to each other than to that of the He atom. This can be attributed to the fact that the dominant contribution to the HHG yield comes from the valence np_0 orbital in both Ne and Ar atoms, whereas only the $1s$ orbital contributes to HHG in the case of He. In the following sub-
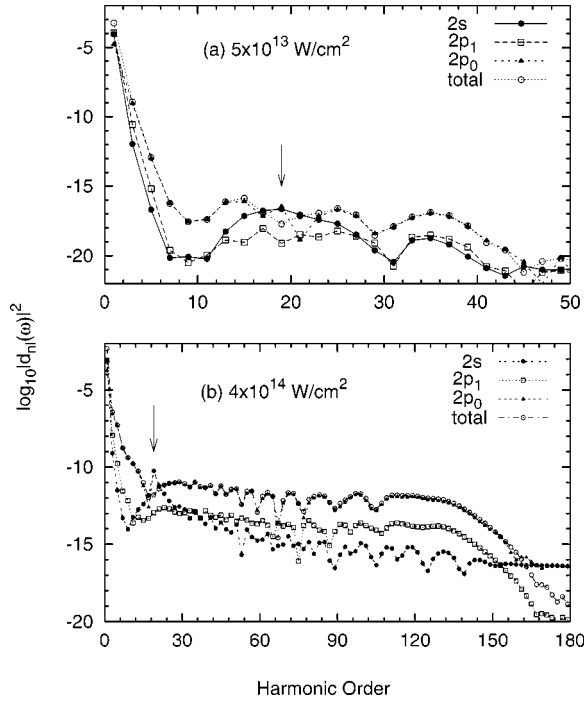
FIG. 6. The HHG power spectrum and the partial contribution from individual valence electron ($2s$, $2p_0$, and $2p_1$) of Ne atoms in pulsed laser fields with peak intensities: (a) 5×10^{13} W/cm^2, and (b) 4×10^{14} W/cm^2. Other laser parameters used are the same as those in Fig. 5.
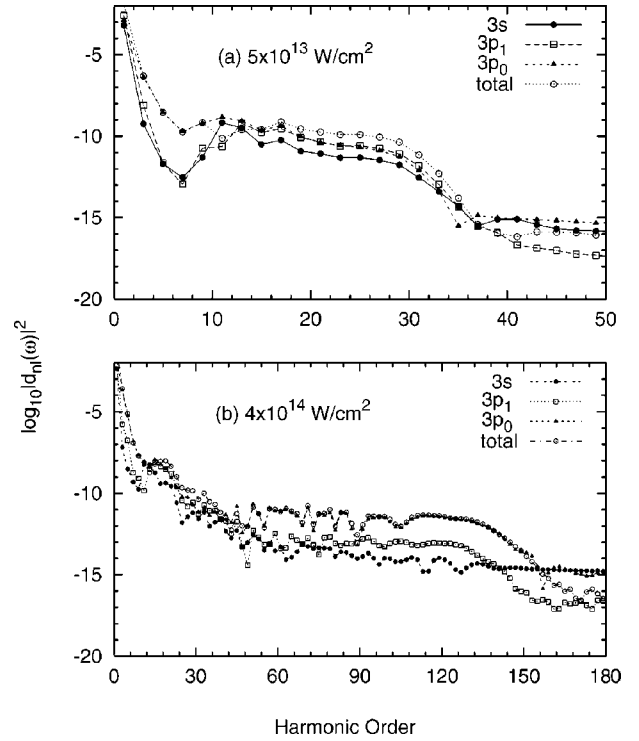

FIG. 7. The HHG power spectrum and the partial contribution from individual valence electron ($3s$, $3p_0$, and $3p_1$) of Ar atoms in pulsed laser fields. The laser intensties and field parameters used are the same as those in Fig. 6.

section, we analyze the partial contribution from the individual valence electron in the Ne and Ar atoms in more details.

A. HHG of Ne atoms: Analysis of subshell contributions

Figures 6(a) and 6(b) show the HHG power spectra of Ne in two different laser peak intensities: (a) 5×10^{13} W/cm^2 and (b) 4×10^{14} W/cm^2. For each case, we show the partial contribution from each valence electron subshell, namely, $2s$, $2p_0$, and $2p_1$. Note that the power spectrum in Eq. (12) is a coherent summation of each spin-orbital contribution, the relative phase of the induced dipole of each spin-orbital plays an important role when the induced dipoles are in the same order. In principle, we cannot separate each orbital contribution. The individual spin-orbital power spectrum presented in Fig. 6 (as well as in Fig. 7) is obtained by the square of the Fourier transform of the corresponding spin-orbital induced dipole, $d_{i_\sigma}(t)$, in Eq. (10). We note that the $2p_0$ electrons make the dominant contributions to the total HHG yield for both intensities. Such behavior arises from the fact that $2p_0$ has the lowest ionization potential and its unperturbed electron density is parallel to the electric field. For the lower-intensity case, Fig. 6(a) shows that the $2s$ contribution to harmonic intensities is about the same order of $2p_1$ contribution for lower and higher harmonics, while for the harmonics in the intermediate plateau regime, $2s$ has higher contribution. This may be attributed to the (19 photon) near-resonant $2s \rightarrow 2p_0$ excitation as evidenced by the abnormal high-harmonic yield of the 19th harmonic. When

the laser intensity becomes considerably stronger [Fig. 6(b)], the $2s$ contribution is roughly of the same order as that of $2p_1$ in the early part of the plateau ($n < 60$), except nearby the 19th harmonic where the $2s$ harmonic intensities are enhanced due to $2s \rightarrow 2p_0$ resonant excitation. For higher harmonics, the $2p_1$ contribution becomes considerably higher than that of $2s$. However, the HHG yield from both $2s$ and $2p_1$ orbitals are considerably lower than that of $2p_0$ orbital and thus they do not contribute to the total HHG power spectrum in a significant way.

B. HHG of Ar atoms: Analysis of subshell contributions

The corresponding results for Ar are shown in Figs. 7(a) and 7(b) for the same two laser intensities in Fig. 6. In the weaker field case [Fig. 7(a)], $3p_0$ and $3p_1$ have a similar order of contribution to the whole plateau harmonics (from 13th till the 35th harmonic), and the corresponding $3s$ contribution is considerably smaller. There is no multiphoton resonant excitation effect in this case. In the lowest-harmonic regime dominated by multiphoton mechanism, we see that $3p_0$ is the primary contributor to harmonic emission. In the stronger field case [Fig. 7(b)] the most salient feature is that the $3p_0$ electrons makes the largest contribution to the whole range of harmonics, followed by the $3p_1$ and then $3s$ electrons. The relative contribution of the individual subshell is particularly apparent in the plateau regime where the total HHG yield is dominated by the $3p_0$ orbital. This latter pattern suggests that it is advantageous to use atoms or mol-

ecules with oriented valence orbital(s) (parallel to the electric field) to achieve higher HHG yield and longer plateau.

C. Effects of self-interaction correction in the HHG study

Finally, it is instructive to make some comments regarding the effects of SIC in the HHG calculations, that is the comparison of the present TDOEP/KLI-SIC with time-dependent local-density approximation (TDLDA) (without SIC). Some preliminary comparison has been made for the case of He in one of our recent studies of HHG [7]. Due to the lack of correct long-range Coulombic potential, the local-density approximation (LDA) electrons are too loosely bound. For example, the LDA, OEP/KLI-SIC, and experimental values for the binding energy of $3p$ electron of Ar are, respectively, 0.382, 0.580, and 0.580 a.u., while the corresponding values for the Ar $3s$ electron are 0.883, 1.112, and 1.077 a.u. From the previous He calculations [7], we found that the HHG cutoff of TDLDA calculations tends to occur earlier than that of TDOEP/KLI-SIC. Further the TDLDA HHG intensities in the plateau regime are significantly (2–3 orders) higher than those of TDOEP/KLI-SIC. Such differences may be attributed to the typical behavior of looser LDA electrons versus the tighter bound OEP/KLI-SIC electrons, namely, an atom with smaller ionization potential in general tends to produce a higher HHG plateau and earlier cutoff. For quantitative prediction of the HHG spectrum, it is thus essential to include SIC so that both the atomic structure and the long-range potential are more accurately treated than in the present paper. For more complex atoms such as Ne and Ar, we expect similar behavior of the total HHG intensities will prevail. As for the subshell contributions, we expect the dominant contributor to TDLDA HHG will be the $2p_0$ orbital for Ne and the $3p_0$ orbital for Ar, which is the same as that in TDOEP/KLI-SIC. This is because these np_0 electrons have the lowest-binding energies and their electron orbital orientations are parallel to the electric-field direction. A more detailed and systematic study of the effect of SIC will be investigated in the future.

V. CONCLUSION

In conclusion, we have presented in this paper a TDDFT/OEP-SIC study of the multiphoton ionization and HHG processes of He, Ne, and Ar atoms in intense pulsed laser fields. All the valence electrons are treated explicitly and the electron correlation is included. The results reveal instructive and qualitatively different behavior for different atom and different laser intensity. We have also presented a detailed analysis of the contributions from the individual valence subshell. Three main factors are identified for accounting the observed phenomena, namely, the relative binding energy and the orientation of the electron density of individual valence electron orbital, and the multiphoton resonant excitation effect. Among the various valence orbitals, we found that the np_0 valence electrons make the dominant contributions to both ionization and HHG processes in strong laser fields. Such electrons have the special features of both low-binding energy and oriented electron-orbital (parallel to the electric-field polarization), leading to higher HHG emission and more extended plateau. Further study of the nonlinear response of oriented targets to strong fields will be pursued in the future.

[1] See, for example, L.S. Cederbaum, K.C. Kulander, and N.H. March, *Atoms and Molecules in Intense Fields* (Springer, New York, 1997).

[2] Z. Chang, A. Rundquist, H. Wang, M.M. Murnane, and H.C. Kapteyn, Phys. Rev. Lett. **79**, 2967 (1997).

[3] C. Spielmann, H. Burnett, R. Sartania, R. Koppitsch, M. Schnurer, C. Kan, M. Lenzner, P. Wobrauschek, and F. Krausz, Science **278**, 661 (1997).

[4] M. Schnürer, Ch. Spielmann, P. Wobrauschek, C. Streli, N.H. Burnett, C. Kan, K. Ferencz, R. Koppitsch, Z. Cheng, T. Brabec, and F. Krausz, Phys. Rev. Lett. **80**, 3236 (1998).

[5] J.L. Krause, K.J. Schafer, and K.C. Kulander, Phys. Rev. A **45**, 4998 (1992).

[6] A. L'Huillier, K.J. Schafer, and K.C. Kulander, J. Phys. B **24**, 3315 (1991).

[7] X.M. Tong and S.I. Chu, Phys. Rev. A **57**, 452 (1998).

[8] X.M. Tong and S.I. Chu, Int. J. Quantum Chem. **69**, 293 (1998).

[9] R.G. Parr and W.T. Yang, *Density-Function Theory of Atoms and Molecules* (Oxford University Press, New York, 1989).

[10] A.D. Becke, Phys. Rev. A **38**, 3098 (1988).

[11] C. Lee, W. Yang, and R.G. Parr, Phys. Rev. B **37**, 785 (1988).

[12] J.P. Perdew and Y. Wang, Phys. Rev. B **33**, 8800 (1986).

[13] X.M. Tong and S.I. Chu, Phys. Rev. A **55**, 3406 (1997).

[14] J.B. Krieger, Y. Li, and G.J. Iafrate, Phys. Lett. A **146**, 256 (1990).

[15] R.T. Sharp and G.K. Horton, Phys. Rev. **90**, 317 (1953).

[16] J.D. Talman and W.F. Shadwick, Phys. Rev. A **14**, 36 (1976).

[17] J. Chen, J. Krieger, Y. Li, and G. Iafrate, Phys. Rev. A **54**, 3939 (1996).

[18] X.M. Tong and S.I. Chu, Phys. Rev. A **57**, 855 (1998).

[19] C.A. Ullrich, P.G. Reinhard, and E. Suraud, Phys. Rev. A **62**, 053 202 (2000).

[20] C.A. Ullrich, U.J. Gossmann, and E.K.U. Gross, Phys. Rev. Lett. **74**, 872 (1995); C.A. Ullrich and E.K.U. Gross, Comments At. Mol. Phys. **33**, 211 (1997).

[21] X.M. Tong and S.I. Chu, Chem. Phys. **217**, 119 (1997).

[22] X.M. Tong and S.I. Chu, Phys. Rev. A **58**, R2656 (1998).

[23] X.M. Tong and S.I. Chu, J. Phys. B **32**, 5593 (1999).

[24] X.M. Tong and S.I. Chu, Phys. Rev. A **61**, 012802(R) (2000).

[25] S.-I. Chu and X.M. Tong, Chem. Phys. Lett. **294**, 31 (1998).

[26] X.M. Tong and S.I. Chu, Phys. Rev. A **61**, 031401(R) (2000).

[27] J. Wang, S.I. Chu, and C. Laughlin, Phys. Rev. A **50**, 3208 (1994).

[28] G. Yao and S.I. Chu, Chem. Phys. Lett. **204**, 381 (1993).

[29] X.M. Tong and S.I. Chu (unpublished).

[30] P.B. Corkum, Phys. Rev. Lett. **71**, 1994 (1993).

[31] K.C. Kulander, K.J. Schafer, and J.L. Krause, in *Super-Intense Laser-Atom Physics*, Vol. 316 of *NATO Advanced Studies Institute, Series B: Physics* (NATO ASI B316), edited by P. B. Piraux *et al.* (Plenum, New York, 1993).